HPD AND MAPMT - SEGMENTED PHOTON DETECTORS FOR HEP AND BEYOND

C. JORAM

CERN, Physics Department, CH-1211 Geneva 23, Switzerland
email Christian.Joram@cern.ch

We review the basic principles and some performance limits of Multi Anode Photomultiplier Tubes and Hybrid Photon Detectors. Applications in High Energy Physics and other fields illustrate the potential and limitations of some state-of-the-art devices.

1. Introduction

The need for high sensitive and finely segmented photon detectors is characteristic for current and future High Energy Physics (HEP) experiments, both at hadron and lepton machines. There are essentially three main domains which lead to very large numbers of detection channels and therefore require cost effective readout options:

- Calorimetry - the readout of scintillator crystals or plastic scintillators
- Cherenkov detectors - the detection of very low light levels in Ring Imaging Cherenkov (RICH) counters
- Tracking - the readout of a scintillating fiber tracker.

The following characteristics are usually key requirements, while the weighting among them depends of course on the specific application: capability to detect very low light levels, linearity of the signal amplitude, often even single photons, high response speed (within one bunch crossing interval of the collider), fine segmentation, high active area fraction and, last but not least, cost effectiveness.

Applications in non-HEP, like astrophysics and medicine, have partly very similar requirements and consequently make use of similar photodetectors. The quality of neutrino experiments like Super-Kamiokande or SNO and air shower Cherenkov telescopes like MAGIC or CLUE is directly

correlated with the performance of their photodetectors. The market volume in the medical imaging domain, e.g. Positron Emission Tomography (PET) and Single Photon Emission Computed Tomography (SPECT), exceeds physics applications by far and clearly has a strong impact on the R&D programmes of industrial photodetector suppliers. Nevertheless the HEP community is continuing to perform new developments, partly in collaborative efforts at research centers like CERN, partly in collaboration with industry. The result are photodetectors with characteristics optimally matched to the requirements of the physics experiment.

Photodetectors can be classified in vacuum based, gas based and solid state devices. This article deals only with segmented vacuum based photodetectors, namely Hybrid Photon Detectors (HPD) ([1,2] and references therein), often also - misleadingly - called Hybrid Photodiodes, and Multi Anode Photomultiplier Tubes (MAPMT) [3]. In both devices the conversion of a photon into a photoelectron occurs by means of external photoeffect in a semi-transparent or reflective photocathode. The photoelectron is ejected from the cathode into the vacuum. In order to achieve a signal large enough to be detected (i.e. discriminated from the noise of the readout chain), appropriate multiplication mechanisms need to be applied. Those differ fundamentally in HPDs and MAPMTs.

Before we describe the principle of operation of HPDs and MAPMTs, their performance and various applications, we briefly recall the main features of gas based and solid state detectors.

- Gas based photodetectors
  The photon to be detected ionizes either the counting gas of the photodetector (e.g. Methane/Ethane with a small admixture of TMAE or TEA) or a solid photocathode (e.g. CsI) by external photoeffect (quantum efficiency $< 50\%$). The photoelectron is then multiplied in an avalanche, which takes place in a region with sufficiently high electric field (e.g. MWPC or GEM structures). Operation at atmospheric pressure allows to build flat large area detectors, which are practically immune even to very strong magnetic fields. The threshold of currently available robust photocathodes (CsI) restricts the use of these detectors to the deep UV region.
- Solid state detectors
  The absorbed photon generates an electron-hole pair in a (partially) depleted silicon (pn) diode. The quantum efficiency is high ($>$ 50%) thanks to the exploitation of the internal photoeffect. In a

simple p-i-n diode structrue the current related to the separation of the e-h pair results in a detectable photon current (gain $G = 1$). Avalanche photodiodes (APD) have an additional high electric field region in which an avalanche mechanism leads to gain values of 50 to 1000. Recently developed Geiger mode APDs [4,5,6] operate in quenched (i.e. controlled) Geiger mode and achieve gain values in the 10^6 region, however on the expense of a high dark count rate and limited linearity.

2. Hybrid Photon Detectors

Similar to most photomultiplier tubes, Hybrid Photon Detectors consist of a vacuum envelope with a transparent front window. The photoelectrons are emitted from the thin photocathode into the vacuum where they are accelerated by a potential difference ΔV of the order of 10 to 20 kV onto a silicon sensor, which serves as anode and which is usually kept at ground potential. The electric field between cathode and anode can be shaped by means of electrodes in order to obtain certain electron-optical properties, e.g. a linear demagnification between the photocathode and the silicon sensor. The absorbed kinetic energy of the photoelectron gives rise to the creation of electron-hole pairs, which in the depleted silicon sensor results in a detectable current pulse.

Depending on the specific application HPDs can be produced with various photocathode and window types. The mose frequent combinations are bialkali (K_2CsSb) and multialkali (NaKCsSb) cathodes on glass or quartz windows. For special applications also solar blind UV cathodes, like CsTe or Rb_2Te, and window materials like sapphire (Al_2O_3) complement the range.

Segmenting the silicon sensor in diode strips, pixels or pads which are read out individually results in a position sensitive HPD. The gaps between the doping implantations, which are usually of the order of 20-50 μm, do not lead to dead zones but are fully sensitive. The phtotoelectron detection efficiency is therefore in general uniform over the complete silicon sensor surface. The spatial resolution of the HPD is however not only determined by the granularity of the sensor but also by its electron optical properties. The *classical* HPD designs are illustrated in Fig. 1. Distortions of the electric field (due to geometrical imperfection of the electrode structure) as well as the distribution of the emission angle and energy of the photoelectrons at the photocathode lead to a limited resolution, characterised by

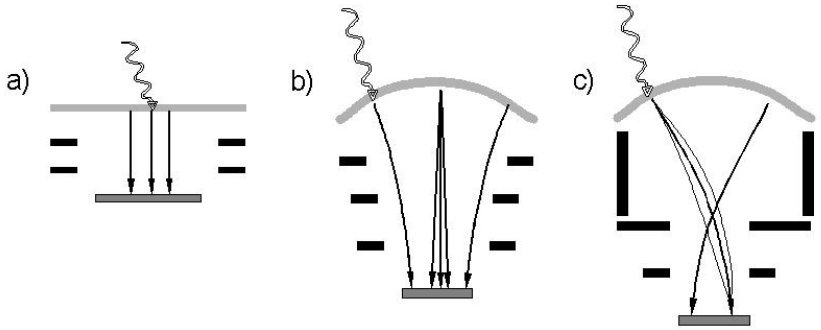

Figure 1. Classical HPD types: a) proximity focused; b) fountain focused; c) cross focused.

the point spread function σ_{ps}. It scales like $\sigma_{ps} \approx \sqrt{L_{CA}/\Delta V}$, where L_{CA} is the distance between cathode and anode and ΔV the applied potential difference.

The electrostatics of cross-focused HPDs (design c) in figure x) acts like an electrostatic focusing lens which is able to partly corrects these aberrations. Carefully designed optics achieve point spread functions below 50 μm.

The electron optical properties of HPDs are in general very sensitive to magnetic fields. While a proximity focused HPD even profits from the presence of a purely axial field (reduction of the point spread function, see below), the operation of fountain and cross-focused HPDs is significantly compromised both by axial and transverse fields above a few 10 Gauss. Image rotation (in axial fields) as well as shift and expansion (in transverse fields) are observed. Appropriate mu-metal shielding and offline corrections can extend the operability range to values below $\approx$ 50 Gauss.

2.1. *Silicon sensor and gain mechanism*

In an HPD the accelerated photoelectrons bombard the silicon sensor and penetrate it to a depth of a few μm. The number of created electron-hole pairs per photoelectron, i.e. the gain of the device, is given by

$$G = (\Delta V - E_0)/W_{e-h} \tag{1}$$

with $W_{e-h} = 3.6$ eV being the average energy needed for the creation of a single electron-hole pair in silicon. E_0 describes the energy loss ($\approx$ 1-2 keV) in non-active material layers of the Silicon detector (aluminium

contact layer, n^+ layer). The design of the silicon sensor has therefore to be optimised for minimal dead layer thickness. For a potential difference $\Delta V = 20$ kV a gain of about 5000 is achieved. The small penetration depth of the electrons results in relatively fast signals. Sub-ns rise- and fall-times have been demonstrated under optimized conditions [7], although a 300μm thick standard p-in-n sensor, in which the signal is essentially due to hole collection, does not achieve this performance. The charge amplification process is purely dissipative and non-multiplicative. The observed gain spread is given by

$$\sigma_G = \sqrt{ENF \cdot G \cdot F \cdot n_{pe}} \oplus ENC \tag{2}$$

where $F \approx 0.1$ denotes the Fano factor for silicon and $n_{pe} = 1, 2, 3...$ the number of photoelectrons. The excess noise factor ENF for such a dissipative process is essentially 1. In practice the Poissonian term (left) is much smaller than the equivalent noise charge ENC of the readout electronics (pedestal noise) which will finally determine the energy resolution of the HPD.

If an HPD is to be used to detect single photons, the relatively small gain demands low noise readout electronics. A well designed readout system with a RMS pedestal noise of a few hundred electrons (ENC) leads to a signal to noise ratio (SNR) above 10 for single photoelectrons. This is the basis for the impressive photon counting capabilities of HPDs, i.e. the ability to distinguish between single, double, triple etc. photon hits.

2.2. *Limitations*

Two effects, which are inherent to the detection of a low energy ($10-20$ keV) photoelectron in silicon, pose certain limitations to the HPD peformance: Backscattering of the photoelectron from silicon and charge sharing between readout cells (see Fig. 2.1).

2.2.1. *Backscattering*

The probability α_{Si} that the photoelectron is backscattered from the silicon sensor into the vacuum is ≈ 0.18. Backscattered electrons deposit only a fraction $0 \leq \varepsilon \leq 1$ of their kinetic energy in the silicon. This effect leads to a number of consequences:

- The distribution of the single photoelectron signal amplitude exhibits a fairly flat low energy shoulder which extends to zero.

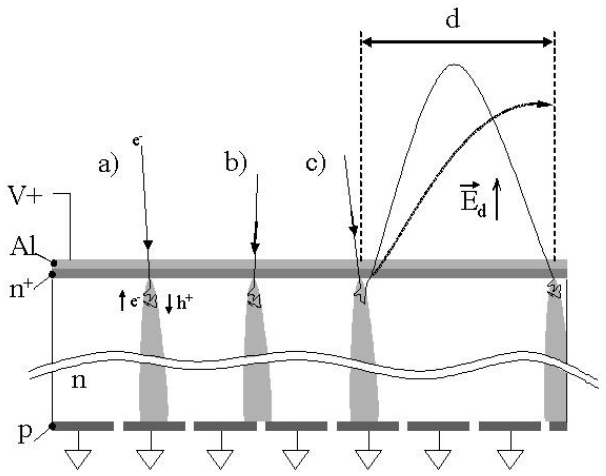

Figure 2. Schematic representation of the electron detection process at the silicon sensor. a) Full energy deposition and charge detection on one pad; b) Full energy deposition, charge shared by two pads; c) Partial energy deposition and subsequent backscattering with loss or re-detection of electron.

This limits the single photoelectron detection efficiency to $\varepsilon_{det} = 1 - \alpha_{Si} \cdot (n_\sigma / SNR)$, with n_σ being the value of the pedestal noise cut, expressed in number of sigmas. Typical values (SNR $\approx$ 10, $n_\sigma \approx 4$) lead to a detection efficincy in the 90 - 95% range.

- Depending on its emission angle and energy, the backscattered electron can hit another cell of the silicon sensor and therefore appear as cross talk. A simple ballistic consideration shows that the maximum range is $2L_{CA}$. If the HPD is operated in a magnetic field, the trajectories of the backscattered electron become rather complex [1]. An axial magnetic field is in general benificial in this respect as it confines the trajectory to a narrow helix such that the electron is often re-detected in the same cell.
- For higher light levels ($n_{pe} > 10$) the back scattering effects leads to a quasi combinatorial continuum and starts to wash out the photoelectron peaks. If we assume the fractional energy distribution ε to be flat and the backscattered electron be lost, the signal distribution for n_{pe} photoelectrons has its maximum at $(1 - \alpha_{Si}/2)n_{pe}$ and is slightly broader (4 - 5%) than the Poissonian value $\sqrt{n_{pe}}$.

2.2.2. *Charge sharing*

Most of the current HPD designs make use of a back bombarded silicon pn diode structure. The holes, generated close to the n^+ back implantation, need to drift through almost the full thickness of the sensor (typically 300 μm) before they reach the segmented p^+ implants. Due to transverse diffusion along the drift through the bulk, the charge cloud arrives as a Gaussian distribution with a width of the order of $\sigma = 10$ μm. In case of very small pixels (<50 μm) the total detectable charge will be shared by several pixels where the charge detected by the individual pixel may fall below the detection limit (pedestal noise cut or discriminator threshold). Studies with the LHCb Pixel HPD (see section 2.4.2) indicate substantial charge sharing in the direction of the 62.5 μm pixel pitch. Depending on the threshold of the readout electronics a double cluster probability of up to 20% is found.

2.3. *HPD fabrication*

HPDs are generally produced by means of an external process [8], i.e. cathode and anode are physically separated while the processing of the photocathode takes place. This method minimizes the pollution of the tube components and, most important, of the silicon sensor with alkali vapors. Two variations of this principle have been implemented, each of them having specific advantages and problems: (1) The HPD body is joint to the baseplate which carries the silicon anode and after the photcathode processing is in-situ sealed by the entrance window; (2) The body is pre-sealed to the entrance window and the in-situ sealing happens on the level of the base plate. In both cases pure indium or low melting indium alloys are used as sealing media. All tube components need to be vacuum baked at elevated temperature. The entrance window, acting as substrate for the photocathode, requires a thorough high temperature bakeout ($\geq 300^o$C) for optimum cleanliness. In view of a long term operation of the HPD care has to be taken in the selection of the materials in order to minimize the outgasing rates. Above a certain number of channels (a few hundreds) it becomes impractical to readout the segmented silicon sensor through individual vacuum feedthroughs. In this case the readout electronics has to be integrated in the vacuum envelope. Obviously this increases the degree of fabrication complexity and demands tight quality assurance measures in order to maintain the production yield in reasonable limits. For tubes with very high channel number (> 1000) low power consumption is a must to

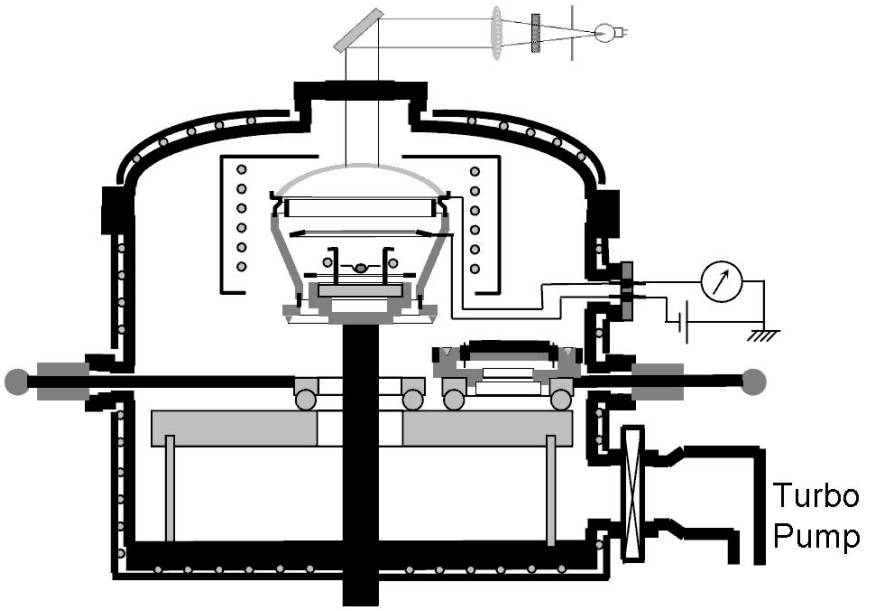

Figure 3. Schematic view of the HPD processing facility at CERN.

keep the operation temperature of the electronics in a safe range.

2.4. *Recent HPD developments in HEP*

The following two develpments were initially launched as competing R&D programmes for the readout of the RICH detectors of LHCb [9]. Fast (40 MHz) and finely segmented (≈2.5 mm) photodetectors were required, operating in the visible and near UV domain and covering the large focal plane (2.9 m^2) with the highest possible filling factor.

2.4.1. *The 5-inch Pad HPD*

The early versions of the Pad HPD consisted of a cylindrical vacuum glass envelope of 127 mm diameter with a spherical entrance window made of borosilicate glass. A visible light transmittive bialkali photocathode (K_2CsSb) is vacuum evaporated on the inside surface of the window. The photoelectrons are accelerated by a potential difference of the order of 20 kV onto a silicon sensor of 50 mm active diameter. Focusing ring electrodes produce a fountain-like electrostatic field geometry, which results in a linear

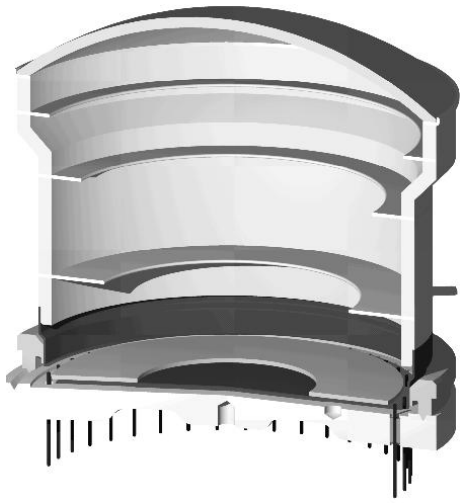

Figure 4. 3D drawing of the ceramic 5-in. HPD.

demagnification of ≈ 2.5 over the full geometrically accepted diameter of 114 mm. The silicon sensor consisting of 16 sectors with in total 2048 pads (1×1 mm^2) is mounted on a 4-layer ceramic printed circuit board. Wire bonds feed the signals to 16 VA [23] analogue readout chips (128 channels: pre-amplifier, shaper, sample & hold and multiplexer). The Pad HPD is fabricated in a dedicated ultrahigh vacuum facility at CERN which, after adaptation, has also been used for the fabrication of the 10-inch TOM HPD and the PET HPD, discussed below. Numerous Pad HPD prototype tubes were built and fully characterized in lab test benches and various beam set-ups with Cherenkov radiators. The excellent results are documented in several publications [10,11] . Although LHCb decided in favour of the Pixel HPD discussed below, an active development activity is being maintained around the HPD facility at CERN. Currently a Pad HPD version with ceramic tube body, kovar electrodes and quartz entrance window (see Fig. 4 is under development together with the UK company PHOTEK. The ceramic - kovar technology provides higher geometrical precision, which improves the electron optical characteristics. The chosen design has a very thin cathode flange which does not lead to electrical field distortions which otherwise need to be corrected by an additional (bleeder) electrode.

2.4.2. *The Pixel HPD*

The 80 mm diameter HPD [12] employs the cross focusing technique, implemented by means of a ceramic body with sperical entrance window and kovar electrodes. In its current version the image of the 72 mm active diameter S20 photocathode is demagnified by a factor 4.5 onto a silicon pixel sensor consisting of 8192 pixels of 62.5×500 μm^2 each. A binary readout chip is bump bonded to the pixel array, a technology which required extra effort to be made compatible with high temperature vacuum baking. 8 pixels are each grouped together in the readout chip to form a logical super-pixel of 500×500 μm^2. The readout chip [13] is the result of a co-development with the ALICE pixel group. The tube is developed in collaboration with and built by the Dutch company DEP. In lab and beam tests it has proven the required performance for operation in the LHCb RICH environment. Some preliminary results are: Operation at 20 kV at low dark count rate, readout speed 40 Mhz, the applicable threshold 1400 ± 200 (RMS) e^- leads to a single photoelectron detection efficiency of 87%, with more than 95% pixels operational. LHCb has extensively studied the effect of magnetic stray fields on the optics and is confident that a mu-metal shielded tube can be safely operated in fields up to 30 Gauss, although offline image corrections are required.

2.4.3. *The BTeV HPD*

The BTeV experiment is planning to use a RICH with HPD readout like LHCb, however the requirements in terms of segmentation ($\approx$5 mm) and readout speed (Tevatron bunch crosing rate 7.6 MHz) are more relaxed. The BTeV tube [14] is based on the same tube body as the Pixel HPD. The anode consists of a 163 hexagonal pixel sensor (pixel size 1.4 mm FTF), which leads to an effective pixel size at the cathode level of 5.6 mm. The signals are fed out through a ceramic pin grid carrier to external VA electronics adapted to the specific needs (VA_btev). A set of tubes and readout cards have been produced and are intended to be used in a beam test in spring 2004.

2.4.4. *The HPD for the CMS HCAL readout*

The photosensors of the hadronic calorimter (HCAL) of CMS detect light from plastic scintillators which is brought to the sensors by means of wavelength shifting (520 nm) and clean fibers optical fibers. A special require-

ment which eliminates almost any other detector option is the 4 Tesla magnetic field in which the photosensors have to operate. Based on a proximity focused HPD by DEP, a development programme was launched to meet the stringent CMS requirements like gain non-linearity below 5% (in the range 1-70000 pe's !) and total cross-talk below 4%. The CMS HPD [15] exists with two different anode geometries: a 19 hexagonal pixel arrangement (pixel size 5.4 mm FTF) and a 73 hex pixel arrangement (2.68 mm FTF). The acceleration gap between cathode and anode is as small as 3.3 mm, but still sufficient to safely operate the tube at 12 kV. Specific care was taken to minimize the cross-talk, which, in addition to the above mentioned back scattering effect, can also originate from capacitive coupling inside the Si sensor and from optical reflection of light from the silicon sensor back on the photocathode and. The electrical effect was coped with by increasing the thickness of the backside (n^+) Al metallization. The thickness of a thin layer of amorphous silicon, deposited on top of the metallization with a thin Al_2O_3 diffusion barrier in between, can be optimized such that it acts as almost ideal anti-reflection coating.

2.5. *HPD developments outside HEP*

The HPD concenpt was invented and demonstrated more than 40 years ago[16]. Only in 1987 De Salvo[17] practically re-invented the concept and proposed it for scintillator readout in the SSC detector similar to the above described CMS HCAL. However already in the 1970ies and 80ies HPD-like devices were developed for astronomical experiments, e.g. the Faint Object Spectrograph, which is part of the Hubble Space Telescope. In the following we describe two developments, undertaken at the CERN HPD facility, which aim to exploit the attractive features of HPDs for astrophysics and medical imaging.

2.5.1. *The TOM HPD for the CLUE air shower telescope*

The Cherenkov Light Ultraviolet Experiment CLUE [18] comprises a cluster of 9 imaging air Cherenkov mirror telescopes and is situated on the Canarian island La Palma. A major gain in sensitivity is expected from the planned replacement of the TMAE based MWPCs as focal plane detectors by round 10-inch HPDs. In honor of our former collaborator and pioneer of the RICH technique, Tom Ypsilantis, they are called TOM-HPDs. The tube body is produced in classical glass blowing technique and has the same electron-optical concept as the 5-inch Pad HPD. The specific opera-

Figure 5. Photo of a 10-in. and a 5-in. HPD.

tional conditions require the HPDs to be equipped with solar blind Rb_2Te cathodes, evaporated on a quartz window with a very thin conductive underlayer of Indium Tin Oxide (ITO). A first sealed TOM prototype tube has been processed with a bialkali photocathode on a glass entrance window. The characteristics of this world's largest HPD are in good agreement with expectations [19]. The next step towards the final CLUE photodetector is to build a tube with quartz entrance window. The significant mismatch of the thermal expansion coefficients of the quartz window and kovar metal excludes the fabrication of a tube of this size in the classical technique. One option is to join the quartz window to the glass body by means of a vacuum bakeable Indium seal. If this technique turns out to be successful for the above mentioned ceramic 5-inch tube, we will try to adapt it to the TOM HPD.

2.5.2. *The PET HPD for medical imaging applications*

The capability to image the morphology of the body in-vivo by X-rays and Computed Tomography (CT) has changed medicine like no other invention in the 20th century. Nuclear Imaging techniques employing radiopharmaceuticals like SPECT and PET help to detect tumors or provide insight in the molecular functionality of the body. In PET, the distribution of a ^{18}F labelled tracer molecule, usually FDG, is imaged by tomographically reconstructing the essentially collinear 511 keV photon pairs, which are emitted

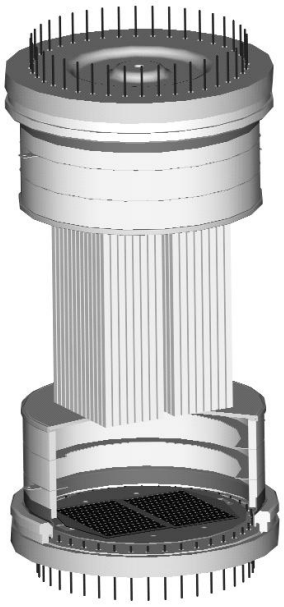

Figure 6. A 3D axial PET camera module.

when the positron from the ^{18}F decay annihilates with an electron in the tissue. Optimum resolution and contrast at minimum patient dose requires a fast and highly senstive scintillation detector, which is able to measure the conversion points of the two gammas in three dimensions. Conventional PET scanners use ring arrangements of small radially oriented scintillators, which are read out on one side by photomultiplier tubes. To limit the parallax error, which is a consequence of the unknown depth of interaction in the crystal (3^{rd} coordinate missing), the length of the scintillator crystal and hence the sensitivity of the scanner is kept small in order to maintain a good spatial resolution.

Our novel concept of a so-called 3D axial PET camera[a] [20] consists of axially oriented arrays long scintillator crystals. A matrix of such crystal bars is read out on both sides by HPDs, of which size and segmentation of the silicon sensor match exactly with the crystal matrix. The axial coordinate (z) is derived from the ratio of the light intensities detected by the two HPDs at the ends of each scintillator matrix, while the transaxial

[a]Patent application filed on 17 July 2002, PCT/EP 02/07967

coordinates (x and y) are directly obtained from the address of the hit crystal. The concept decouples sensitivity and resolution and leads to a full 3D image reconstruction without any parallax effect, uniform over the whole detection volume.

A proximity focused HPD has been designed and a first prototype has been built for such a 3D axial PET camera. A ceramic tube body of 118 mm diameter is capped with a very thin (1.8 mm) entrance window made of sapphire. The silicon sensor is segmented into 216 individual diodes of dimension 4 x 4 mm2 matching the pattern of the planned crystal matrix. A key component of the PET HPD is the auto-triggering analog readout electronics VATA-GP[22]. A special version has been developed which provides the required dynamic range, short shaping time, and sparse readout mode necessary for readout rates in the MHz range.

3. Multi Anode Photomultiplier Tubes

A characteristic feature of photomultiplier tubes is the multiplication process, which is based on the phenomenom of secondary emission. A set of n properly shaped dynodes, maintained on graded potentials, gives rise to the formation of an exponential avalanche with a total charge gain of $G = \prod \delta_i$. The multiplication coefficients of the n dynodes δ_i are approximately identical, however depend on the material type and the applied voltage difference. The signal spread has a contribution from the Poissonian fluctuation of the number of photoelectrons, but also from the fluctuations of the secondary electrons produced at the dynodes (excess noise).

$$\sigma_S = \sqrt{n_{pe} \cdot \{1 + 1/\delta_1 + 1/(\delta_1 + \delta_2) + \cdots + 1/(\delta_1 + \delta_2 + \cdots \delta_n)} \oplus ENC \tag{3}$$

The signal resolution σ_S/S is thus dominated by the fluctuations at the first (and second) dynode and very often exceedes the equivalent noise charge of the readout system.

A PMT with segmented readout requires a dynode system which confines the avalanche in a columnar zone below the emission point of the photoelectron. There are essentially two variants of position sensitive PMTs with this capability.

- PMTs with micro channel plate (MCP) as multiplication stage. The MCP, usually implemented as a microscopic matrix of cylindrical holes in a glass plate, represents parallel quasi-continuous dynodes and obviously confines the avalanches in the holes.

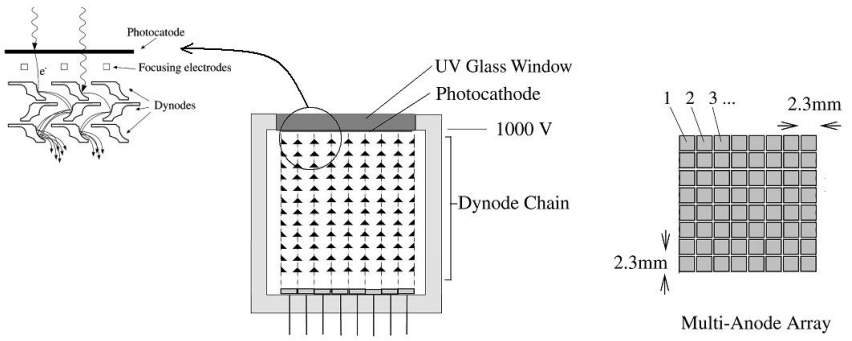

Figure 7. Schematic representation of a metal mesh MAPMT. The anode segmentation corresponds to a Hamamatsu R7600-M64 device.

- PMTs with metal mesh dynodes. A stack of precision machined perforated metal sheets defines vertical channels in which the avalanche is formed.

In both cases the avalanche is detected by two crossed wire planes or, for real 2D readout, by a segmented anode (multi anode) arrangements.

A very recent MCP based development is the Planacon 85011-501 from the company Burle. It has 64 (8×8) channels of 6×6 mm^2 size and excellent timing properties [21].

During the last years metal mesh MAPMTs (see Fig. 7), to a large extent promoted by developments of the company Hamamatsu, became very attractive candidates for applications in HEP, like Cherenkov imaging, and medicine. Positively count the large gain ($\approx 10^6$), the low cross-talk, which is typically on the percent level and the fast signal timing. The latest and since long announced achievement is the so-called Flat Panel PMT (Hamamatsu R8400, 8×8 channels of 6 mm $\square$), which impresses by its tile-like geometry.

3.1. *Limitations*

There are a number of issues which to a certain extent are inherent to the gain mechanism and design principle of metal mesh MAPMTs. The relatively broad pulse height distribution of a (MA)PMT is characteristic for an avalanche multiplication process with a low gain at the first dynode (< 5). Consequently, as demonstrated in Fig. 8 the pulse height distribution extends down to zero, such that a fraction of the signal is lost under the

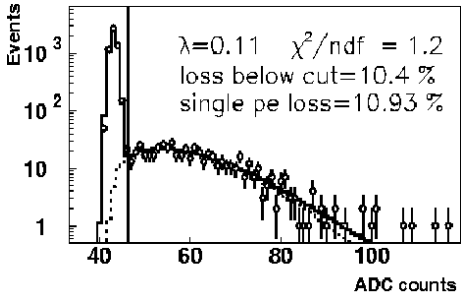

Figure 8. Pulse height spectrum (single photoelectrons) of a MAPMT (R7600-M64) with fast APV25 readout electronics [25]. The peak at ≈ 43 ADC counts corresponds to the pedestal noise of the system.

pedestal noise distribution. Channel-to-channel gain variations of 300% (Fig. 9 and additional differences between tubes of a factor 2 need to be coped with by the readout electronics and/or HV adjustments. It seems that the achievable mechanical precision of the dynode package prevents major improvements in this area. Collecting the photoelectrons in the dynode channels is not a fully efficient process. The sensitivity map of a MAPMT shows therefore clear zones of reduced sensitivity between the pixels and also the pixels themselves show a certain substructure. This effect lowers the effective active area fraction quite significantly below the

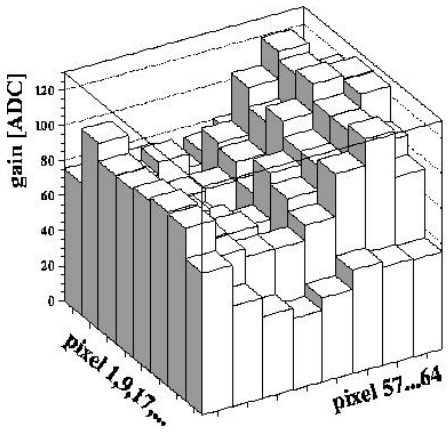

Figure 9. Relative non-uniformity of the gain of a MAPMT (R7600-M64).

nominal values specified by the tube supplier. The mechanical precision and the difficulty to efficiently collect the photoelectrons in the dynode channels may also pose limitations for the achievable granularity. Up to now the smallest realized pixel size is $2 \times 2\ mm^2$. The impact of magnetic fields on the characteristics is less pronounced than for HPDs. The most critical stage, at which B-field related losses occur, is the capturing of the photoelectrons by the dynode channels, but also the gain of the tube is adversely affected.

3.2. *Applications in HEP*

HERA-B was the first large scale HEP experiment which equipped their RICH detector with multi anode PMTs of type Hamamatsu R5900-M4 and M16 [24]. The achieved RICH detector performance and its stability demonstrates that the MAPMT technology is a mature one.

3.2.1. *The MAPMT option of the LHCb RICH*

Encouraged by the HERA-B success, LHCb performs an extensive development program for the readout of the two RICH counters with MAPMTs, in case the above described Pixel HPD option failed to achieve the desired performance. The detector requirements mentioned in section 2.4 made the R5900-M64 (2.1 mm $\square$ pixels) a promising candidate. The modest active area fraction of this tube ($\approx 40\%$) is further reduced when one mounts the tubes with the necessary mu-metal shielding. Therefore, like for HERA-B, a demagnifying system was developed which consists of a single semi-spherical quartz lens mounted in-front of each tube. A beam test with a 3×3 array of MAPMTs showed that the active area could be increased to 85%, of course on the expense that the effective pixel size grew to 3 mm. Various readout options with existing LHC speed front-end electronics (APV25 or Beetle), which were originally developed for silicon sensors, were tested. To match the large PMT signals ($\approx$100 fC) to the dynamic range of the frontends ($\approx$10 fC), an attenuator network was used but found to introduce cross-talk. Running the tube instead at lower HV led to signal loss below threshold. An optimized readout with a modified Beetle chip and a 8-dynode tube is being worked on.

3.3. *Applications in medical imaging*

The availability of position sensitive PMTs has boosted the development of high resolution gamma cameras, e.g. small SPECT devices for scinti-

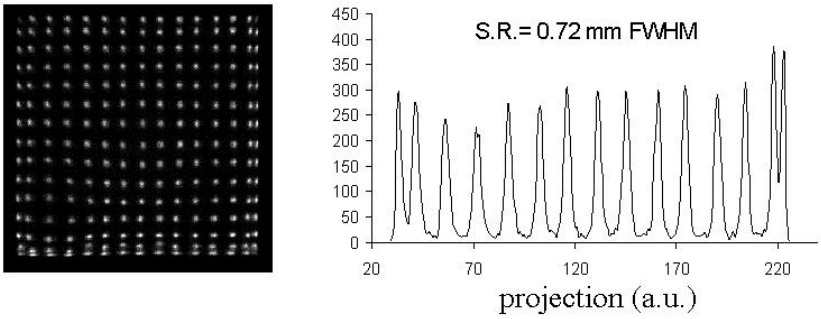

Figure 10. Detection of scintillation light from a 15×15 array of small individual crystals (3×3 mm^2. A Hamamatsu Flat Panel PMT (R8500) is used to readout the crystals through a thin ligh guide.

mammography. This method is based on the gamma decay of ^{99}Tc and complements the classical X-ray mammography. The early detection of breast tumors (below 1 cm) is a challenging goal. Compactness, robustness and an active area fraction as high as possible are key requirements on the photodetector. A state-of-the-art approach consists in coupling an array of small individual scintillators (e.g. $2 \times 2 \times 3$ mm^3 or even smaller) to a position sensitive PMT. A flat thin plate acts as light guide and distributes the light of one crystal over several PMT channels, allowing to unambiguously identify the hit crystal by a centroid calculation. Correction of channel-to-channel gain variation and geometrical distortions leads to impressive results. The Rome group [26,27] uses a Flat Panel PMT to read out scintillation light from a 15×15 array of small individual crystals (3×3 mm^2). Fig. 10 shows the reconstructed centroids when the matrix was exposed to flood field illumination with gammas from a ^{57}Co source. The individual crystals can be resolved unambiguously, although some geometrical distortions remain. The spatial resolution is 0.72 mm (FWHM).

4. Summary and conclusions

Modern and future HEP experiments pose stringent requirements on photodetectors. The huge amount of readout channels requires cost-optimized solutions. On the other hand, the main markets which drive the industrial development of photodetectors are medicine, biology and pharmacology.

In many HEP applications a commercial MAPMT, possibly with optical adaptations (lenses) and well matched readout electronics can lead to fully

satisfactory solutions, equally performant as HPDs.

If ultimate speed ($\approx$ 100 ps) is required, like for the discussed upgrade scenario of the Babar DIRC [21], a (MCP based) MAPMT approach promisses better results than a HPD. The Geiger mode APD is clearly an interesting cadidate in this respect, as well.

The HPD concept provides however a number of advantages like degree of pixelization, signal definition and linearity, uniformity of response and gain, negligible excess noise factor. The modest achievable gain values are easily coped with by modern low noise electronics.

In calorimetry, as already demonstrated in the CMS HCAL approach, these superior characteristics are crucial for the calorimeter performance.

HPDs combine many of the attractive features of vacuum photocathodes and solid state tracking detectors. Unfortunately, when it comes to fabricating devices, also the technical complexity and challenges of the two domains add up.

It remains to be seen, whether technically simple and robust solid state devices like APD and Geiger mode APDs are able to get in the lead.

Acknowledgements

I would like to thank my colleagues at CERN J. Séguinot, A. Braem, E. Chesi and P. Weilhammer for the fruitful collaboration in the various HPD projects. The partly even unpublished material provided by P. Cushman, T. Gys, R. Mountain, F. Müheim, and R. Pani was highly appreciated.

References

1. C. D'Ambrosio and H. Leutz, *Nucl. Instr. Meth. A501 (2003)* 186
2. C. Joram, *Nucl. Phys. B (Proc. Suppl.) 78 (1999)* 407
3. Y. Yoshizawa and J. Takeuchi, *Nucl. Instr. Meth. A387 (1997)* 33
4. P. Bushan et al., *Nucl. Instr. Meth. A504 (2003)* 48
5. B. Dolgoshein. *These proceedings.*
6. I. Musienko. *These proceedings.*
7. G. Anzivino et al. *Nucl. Instr. Meth. A365 (1995)* 76
8. A. Braem et al. *Nucl. Instr. Meth. A502 (2003)* 205
9. LHCb - RICH Technical Design Report. *CERN/LHCC 2000-037,* http://lhcb.cern.ch/rich/
10. A. Braem et al., *Nucl. Instr. Meth. A478 (2002)* 400
11. T. Bellunato et al., *Nucl. Instr. Meth. A504 (2003)* 290
12. M. Campbell et al., *Nucl. Instr. Meth. A504 (2003)* 386
13. P. Riedler et al., *Nucl. Instr. Meth. A501 (2003)* 386
14. R.J. Mountain *Nucl. Instr. Meth. A502 (2003)* 183

15. P. Cushman and Adriaan H. Heering, *ICFA Instrumentation Newsletter, Fall 2002 Issue* www.slac.stanford.edu/pubs/icfa/
16. N. Sclar, "Electron Bombarded Semiconductor as a Circuit Element", Electron Devices Conference, Washington D.C., 1957
17. R. DeSalvo, *Cornell University, preprint, CLNS87-92 (1987)*
18. A. Alexandras et al., Nucl. Instr. Meth. A409 (1998) 488.
19. A. Braem et al., Proceedings of the 9^{th} Pisa meeting on advanced detectors, 2003, *Nucl. Instr. Meth. A*, in press
20. A. Braem et al., Proceedings of the 1^{st} Bajadoz conference, 2003, *Journal of Microscopy, submitted for publication*
21. *J. Va'vra.* These proceedings.
22. A. Studen et al., *Nucl. Instr. Meth. A501 (2003)* 273
23. P. Weilhammer, *Nucl. Instr. Meth. A497 (2003)* 210
24. S. Korpar, *Nucl. Instr. Meth. A502 (2003)* 41
25. F. Muheim, *Nucl. Instr. Meth. A502 (2003)* 52
26. C. Bonifazzi et al., *Nucl. Instr. Meth. A497 (2003)* 179
27. R. Pani et al., *Nucl. Instr. Meth. A513 (2003)* 36